

RESEARCH ARTICLE

Open Access



Major to trace element imaging and analysis of iron age glasses using stage scanning in the analytical dual beam microscope (tandem)

Edward P. Vicenzi^{1,2*} , Thomas Lam¹, Jamie L. Weaver^{2,1}, Andrew A. Herzing², John S. McCloy³, Rolf Sjöblom⁴ and Carolyn I. Pearce⁵

Abstract

Dark and clear silicate glasses formed during an iron age vitrification event \approx 1500 years ago at the Broborg hillfort near Uppsala, Sweden have been analyzed using a scanning electron microscope equipped with a micro-X-ray fluorescence (μ XRF) spectrometer. Correlated μ XRF and electron beam-induced energy dispersive spectrometry (EDS) X-ray maps were collected via stage-scanning at constant velocity. This coupled procedure represents a new approach for the cultural heritage community to conduct analytical studies of archaeometric specimens composed of metal, ceramic, or mixed inorganic/organic materials, where major and trace element compositions are registered in space for areas up to the centimeter-length scale at micrometer-scale resolution. Overview images were used to select areas for EDS beam scan maps correlated with multispectral cathodoluminescence (CL) imaging and co-located quantitative EDS and μ XRF point analysis. Fe, Ca, Mg, Ti, P, Mn, Zr, Zn, and Y are enriched in the dark glass, while Si, Al, K, Na, Ba, Sr, Rb, and Ga are enriched in the clear glass. Unmelted material is comprised predominately of quartz (SiO_2) along with trace apatite ($\text{Ca}_5(\text{PO}_4)_3[\text{Cl},\text{OH}]$) and zircon (ZrSiO_4). Multivariate statistical analysis was used to measure the area fractions of high variance components while lower variance components represented phase mixtures. Differences between calculated melt viscosities for the glass compositions are consistent with field and laboratory observations. Coupled large area EDS and μ XRF imaging shows significant promise for informed selection of higher spatial resolution and higher sensitivity follow-up studies, e.g., those performed using synchrotron analysis.

Keywords: Hillfort, μ XRF, SEM, EDS, X-ray microanalysis, Cathodoluminescence, Quantitative, Vitrification, Silicate glass, Spectrometry

*Correspondence: VicenziE@si.edu

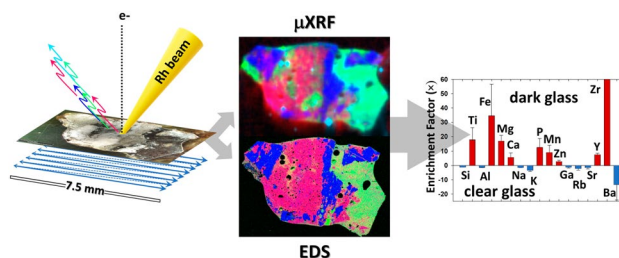
¹ Museum Conservation Institute, Smithsonian Institution, Suitland, MD 20746, USA

Full list of author information is available at the end of the article



This is a U.S. Government work and not under copyright protection in the US; foreign copyright protection may apply 2022. **Open Access** This article is licensed under a Creative Commons Attribution 4.0 International License, which permits use, sharing, adaptation, distribution and reproduction in any medium or format, as long as you give appropriate credit to the original author(s) and the source, provide a link to the Creative Commons licence, and indicate if changes were made. The images or other third party material in this article are included in the article's Creative Commons licence, unless indicated otherwise in a credit line to the material. If material is not included in the article's Creative Commons licence and your intended use is not permitted by statutory regulation or exceeds the permitted use, you will need to obtain permission directly from the copyright holder. To view a copy of this licence, visit <http://creativecommons.org/licenses/by/4.0/>. The Creative Commons Public Domain Dedication waiver <http://creativecommons.org/publicdomain/zero/1.0/> applies to the data made available in this article, unless otherwise stated in a credit line to the data.

Graphical Abstract



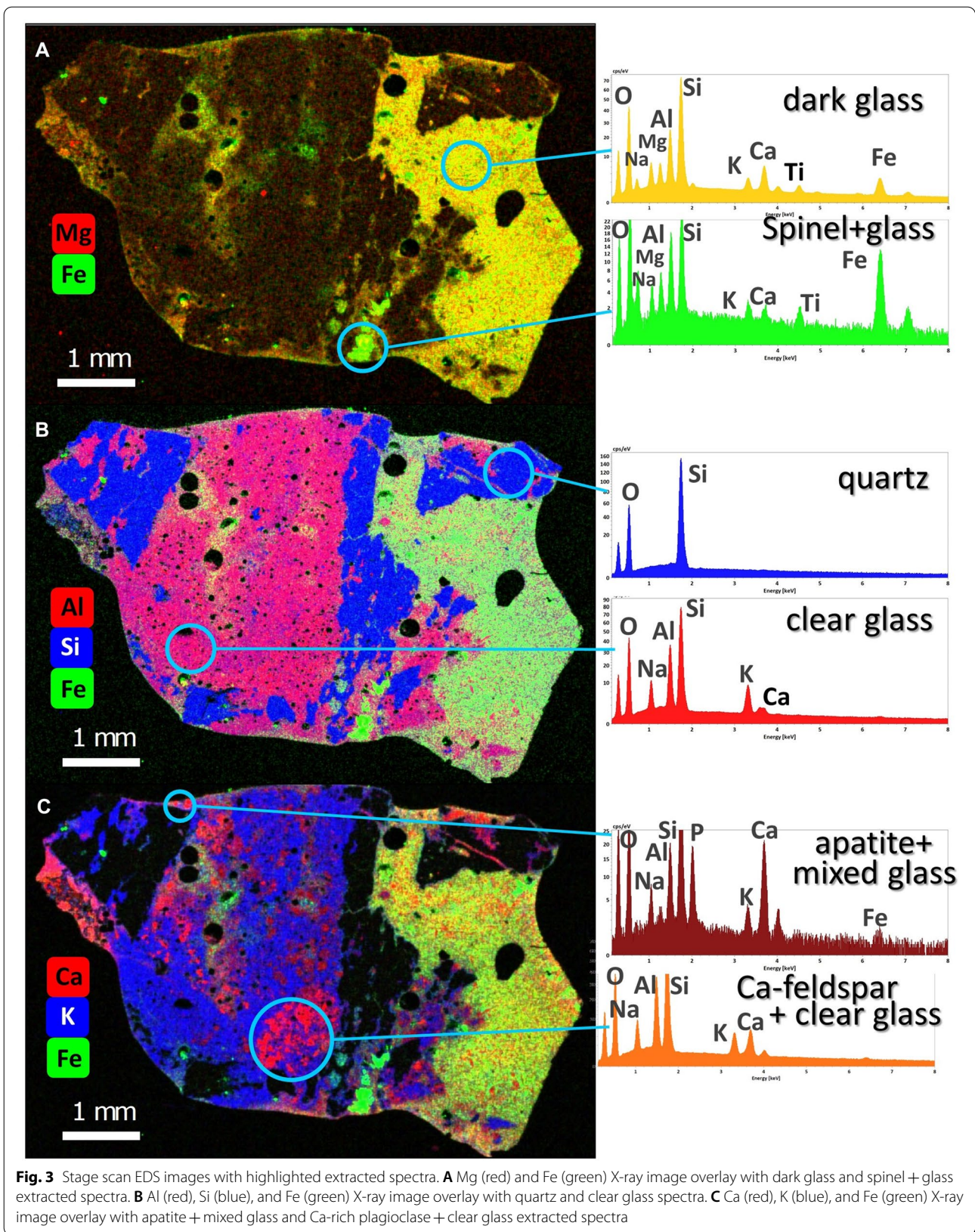
Introduction

Studies combining or comparing results from the scanning electron microscope (SEM) and atmospheric handheld X-ray fluorescence spectrometry (XRF) obtained *ex situ* are not uncommon in the literature [1–6], however XRF systems embedded in electron beam instrumentation represent more rare occurrence [7, 8]. Advances in the field of polycapillary X-ray optics [9–12] enabled the implementation of truly integrated microbeam XRF (μ XRF) into the SEM [13–15]. The principal advantages of the new method in combining the two technologies into one platform includes: high fidelity positioning of the XRF beam via electron beam imaging and coupling energy dispersive spectrometry (EDS) obtained by electron beam excitation complete with low energy X-ray information (e.g., C, N, and O), to higher sensitivity XRF data for moderate to high energy X-ray K lines (e.g., Zn, As and Rb, Sr, Nb). Co-locating the two X-ray spectra that contain: (1) light element information used to identify organics, biological material and metallic corrosion, along with (2) trace element information from heavy elements useful for constraining object provenance, offers a cultural heritage analyst an efficient approach to the compositional documentation of complex artifacts.

Recently, the value of coupled quantitative EDS- μ XRF point analysis to heritage studies has been demonstrated in determining the geological source locality for several highly polished obsidian tablets fabricated during the late Postclassic period in Central Mexico [16]. Analogously, in this effort, we utilize co-located quantitative EDS- μ XRF analysis to examine late iron age glassy material that resulted from a complex vitrification event at the Broborg hillfort in Sweden. The Broborg hillfort is an \approx 1500-year-old fortified archeological site situated approximately 20 km southeast of Uppsala, Sweden (17.9515°E, 59.7556°N) where portions of the fort's stone walls have been reinforced via vitrification [17, 18].

The question of whether hillfort vitrification was the result of hostile interaction, or was intentionally performed by its builders has been part of a long running debate. However in the case of Broborg, the strategic location along a Migration Period waterway, the box-like ventilation structures found within the walls, the evidence for the use of charcoal rather than wood for fuel, and the fact that vitrification covers nearly the entire circumference of the inner rampart, all support the notion that vitrification was used as a deliberate construction technique [19, 20]. The vitrified components at Broborg have been previously analyzed in terms of their socio-historical context [17], as well as pre-Viking, Scandinavian materials' technology development [21, 22], and represents among the earliest known vitrification efforts in Sweden [23].

In this paper, we extend EDS- μ XRF methodology in The Analytical Dual Beam Microscope (TANDeM, hereinafter tandem) by introducing a new archaeometric methodology that is applicable to the study of a wide range of object composition, using X-ray imagery produced by sequential EDS and μ XRF mapping to make informed selection of areas for quantitative analysis. Such maps are acquired by continuous stage scanning of the artifact under stationary electron and photon microbeams and result in X-ray maps that cover centimeters squared in area at micrometer scale resolution. This approach allows for a more complete elemental budget, including major, minor, and trace element images to be evaluated prior to detailed follow-up studies. Post stage-scanning techniques used in this study include cathodoluminescence (CL) imaging that can be sensitive to defects and/or trace impurities [24, 25], and additional electron imaging to co-locate quantitative EDS and μ XRF point analyses to determine element ratios potentially yielding information regarding an object's provenance [16].



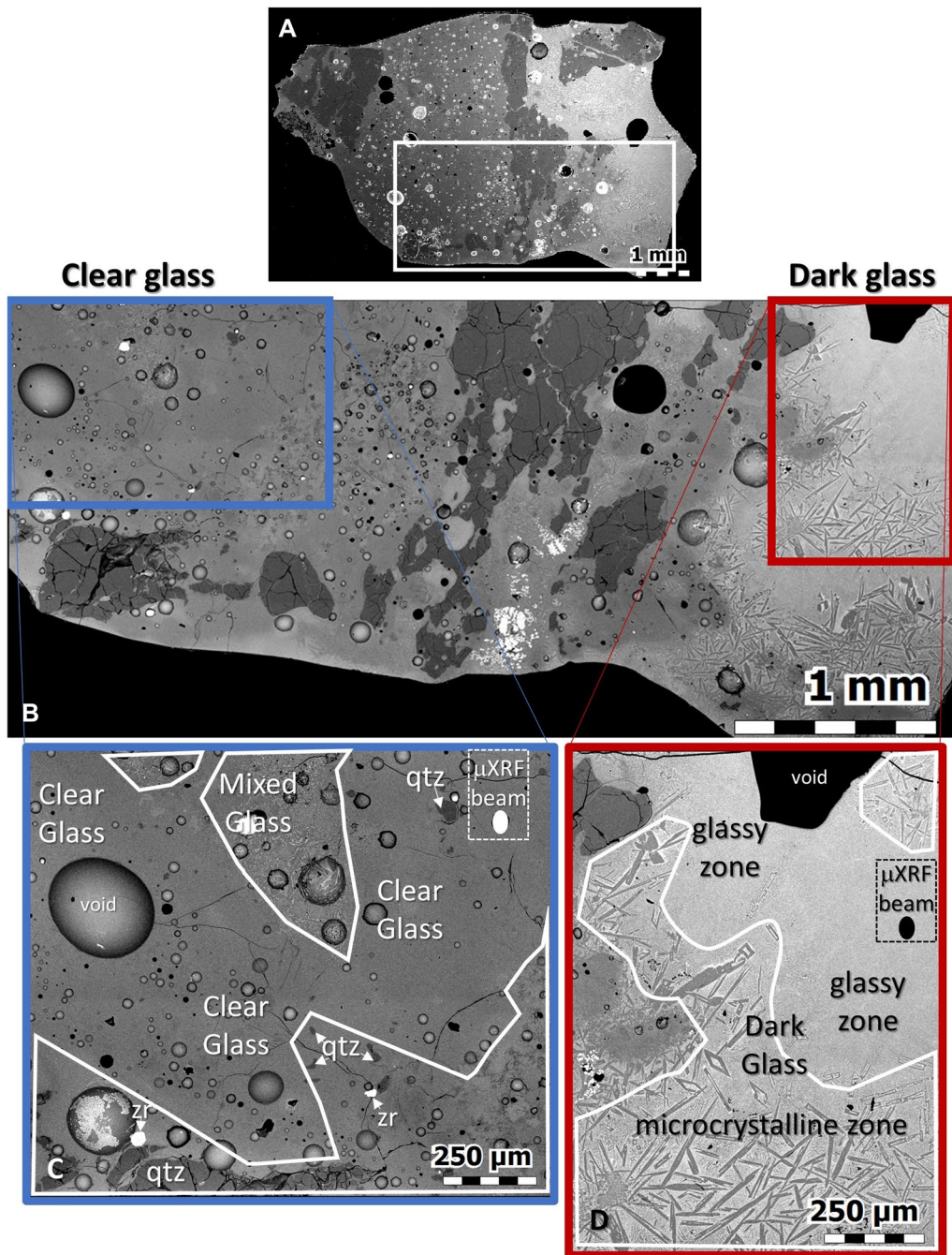
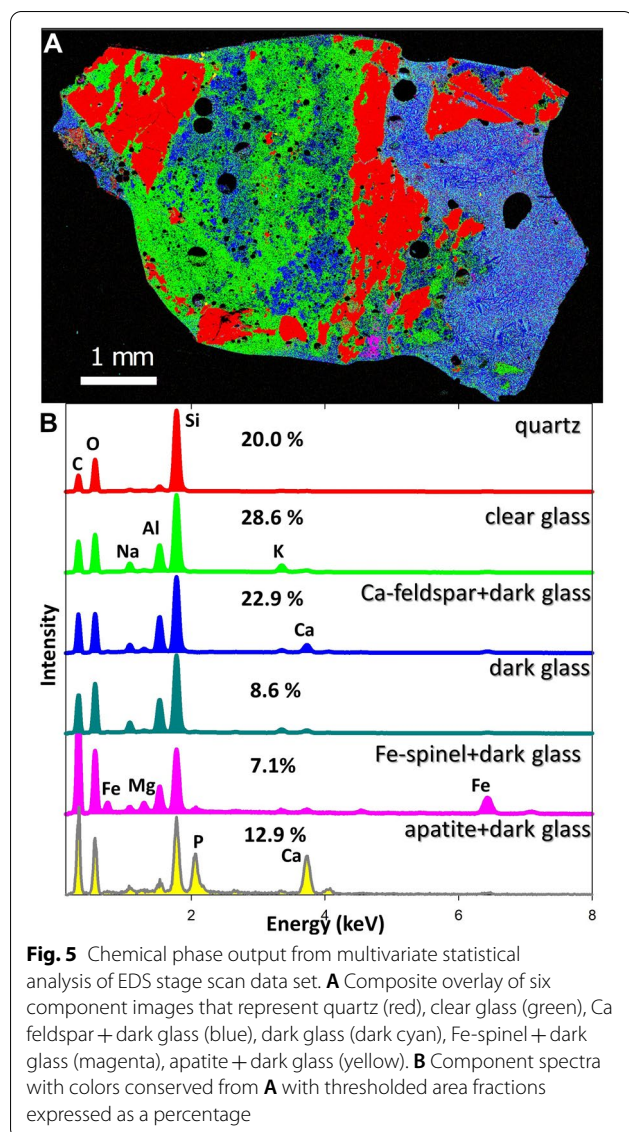


Fig. 4 BSE imagery at differing length scales. **A** Overview image of BB1b. **B** BSE montage of area highlighted by white rectangle in **A**. **C** Higher resolution image of clear glass-rich zone with heterogeneous regions highlighted by white polygons. White arrows highlight residual quartz (qtz) and zircon (zr) (see Additional file 1: Figure S1 for Si and Zr elemental maps). **D** Higher resolution image of dark glass-rich with white polygons outlining microcrystalline zones. Note: White- and black-filled ellipses represent the size of the μ XRF beam for reference within dashed lined rectangles in **C** and **D** respectively

(KAlSi_3O_8) for K and Al (Madagascar), hematite (Fe_2O_3) for Fe (Elba, Italy), synthetic MgO for Mg (Atomerigic Chemetals Corp.), rhodentite (MnSiO_3) for Mn (B.C.,

Canada), albite ($\text{NaAlSi}_3\text{O}_8$) for Na (Amelia, VA, USA), and synthetic $\text{CeP}_5\text{O}_{14}$ for P, while well-characterized materials from the Smithsonian collections were used to



evaluate measurement quality relative to published values (Additional file 1: Table S1) [26, 27].

Micro-XRF spectra were collected using a Rh source operated at 50 kV and 600 μ A. The XRF spot was aligned to the center of the electron beam raster using secondary electron (SE) imaging of an uncoated light microscopy glass coverslip at 3 kV, where the X-ray spot suppresses the yield of SE [14]. The working distance for this lower energy beam differs from that for 15 kV used for EDS analysis by 200 μ m. Given the X-ray optical sensitivity to height differences, imaging and analysis of coupled EDS and μ XRF was performed at 9.8 mm instead of at the standard analytical position of 10 mm. Point analyses and images were collected using unfiltered radiation, and spectra were processed using fundamental parameters (FP) quantification implemented in Bruker Esprit ver. 2.1 [28]. A single data

set with a 100 μ m thick Al source filter was used to evaluate signal to noise ratio differences relative to unfiltered spectra. X-ray emission depths were computed for the dark and clear glass compositions via Monte Carlo simulation for EDS using DTSA II [29] and Bruker XRF Check [30]. Stage scans for EDS and μ XRF X-ray imagery were collected at 2 μ m pixel⁻¹ and 16 μ m pixel⁻¹ using constant velocities of 4.1 mm s⁻¹ and 0.08 mm s⁻¹, respectively.

In order to extract meaningful chemical information from the large size of the EDS hyperspectral dataset, a multivariate statistical analysis (MVSA) treatment was utilized. This type of analysis is commonly employed for hyperspectral datasets when the number of phases is large and/or when many of the phases contain similar elements [31–36]. In such cases, simple elemental maps extracted from the dataset are often difficult to interpret, as many regions of the sample will show similar intensities for each element. By contrast, the MVSA analysis allows the data to be ‘demixed’ so that the individual phases can be spatially isolated even when they share some of the same elemental signatures. The goal of this type of MVSA treatment is to decompose the three-dimensional hyperspectral dataset ($N_{\text{rows}} \times N_{\text{cols}} \times N_{\text{channels}}$) into a smaller number of easily interpretable components which describe the statistically significant features in the data. It is also useful for finding minority phases which might otherwise be lost in the analysis of a large dataset [37]. Additional information regarding the detailed MVSA procedures can be found in Additional file 1: Note (S-1).

The MVSA results were also used to estimate the area fraction of the specimen represented by the various components. To do so, each component image was first segmented using the Otsu method [38], providing the total number of pixels associated with each component. Finally, the fraction of the total number of specimen pixels represented by each component was calculated while ignoring the embedding epoxy and a low energy X-ray absorption artifact.

Results

EDS stage-scan imaging

EDS stage maps of major and minor elements reveal contrast between the dark glass enriched in Fe, Mg, and Ca relative to the clear glass regions enriched in Al and K (Fig. 3). An aggregate of isolated Fe-bearing spinels ($[\text{Fe}^{2+}, \text{Mg}]\text{Al}_2\text{O}_4$) differs in morphology from large regions of irregularly shaped quartz (SiO_2) grains that represents the dominant unmelted crystalline residue (Fig. 3A, B). The dispersed Ca-rich feldspar ($\text{CaAl}_2\text{Si}_2\text{O}_8$ - $\text{NaAlSi}_3\text{O}_8$) is of uncertain origin within the clear glass and is distinct from the feldspar relicts related to the protolith and represents a non-equilibrium

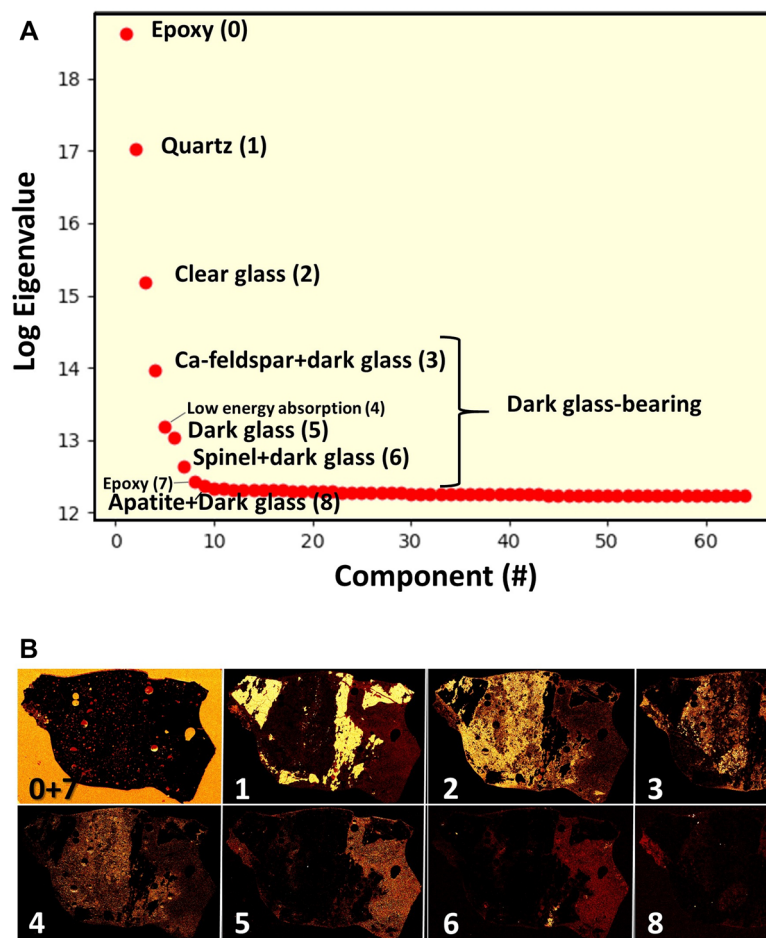


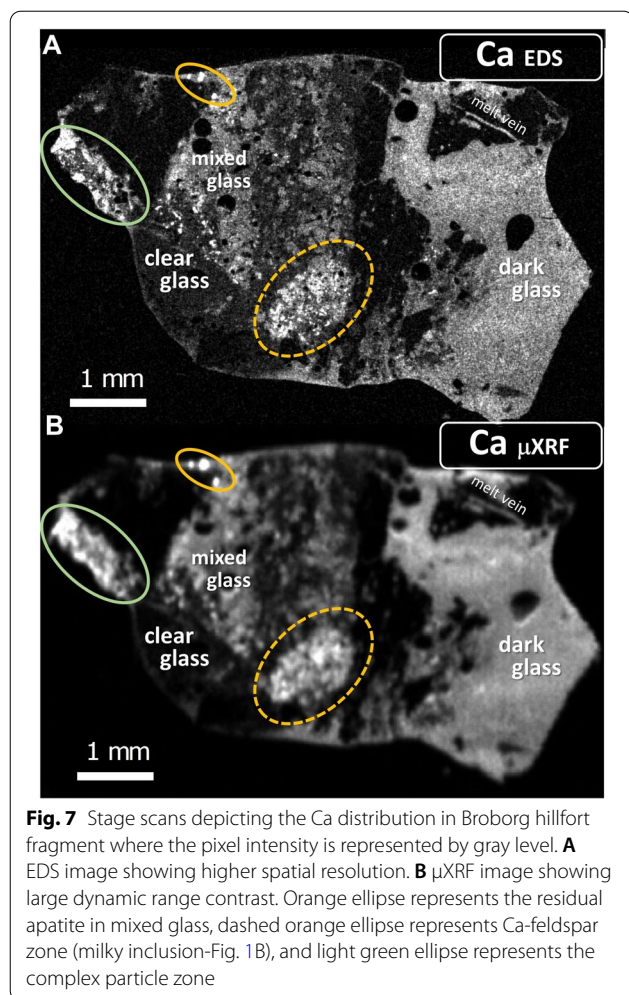
Fig. 6 Multivariate statistical analysis of EDS stage-scan data. **A** Eigenvalue versus component number with non-noise components labeled. **B** Component images with associated component number labels are each scaled individually and shown using a thermal color map to aid interpretation. Horizontal field width = 7.5 mm

composition [39] (Fig. 3C), while trace apatite ($\text{Ca}_5(\text{PO}_4)_3[\text{Cl},\text{OH}]$) grains are likely unmelted crystalline remnants. BSE images showing the clear and dark glasses along with inhomogeneous crystalline zones are depicted in Fig. 4 while correlated elemental maps are shown in Additional file 1: Figure S1. MVSA processing of the EDS stage scan data yields six component images and spectra. The highest variance components, quartz and clear glass, are well-resolved while dark glass is comprised of multiple components, including: (1) feldspar quench crystals in dark glass convolved with Ca-rich feldspars, (2) dark glass, (3) spinel + dark glass, and (4) apatite + dark glass (Figs. 5, 6). The elemental complexity of the dark glass is represented by the four mixed components that account for the lowest variance in the system above the noise level (Fig. 6).

μXRF stage-scan imaging

The overview XRF imaging data set contains an array of elemental information spanning major to minor elements, and a selection of trace elements. This large dynamic range comes at the expense of spatial resolution relative to electron beam-induced data given the tens of micrometer lateral size of the μXRF spot for laboratory-based systems [14]. These differences are illustrated in a side-by-side comparison of registered Ca K line images for EDS and μXRF showing high Ca contrast in three regions of BB1b including a complex particle zone that is part of a follow-up study and is outside the scope of this paper (Fig. 7).

With respect to depth resolution, the physics of X-ray attenuation govern the XRF information depth for a matrix composition [28]. Using a figure of merit of 90% of emitted X-rays, the computed emission depths are divided between major and minor elements and trace



elements in the Broborg glasses (Additional file 1: Figure S2). For low to moderate energy X-ray lines, i.e., Na, Mg, Al, Si, and P, the XRF depth resolutions are estimated to be $< 2.4 \mu\text{m}$ and are similar to those estimated for EDS emission depths obtained by a Monte Carlo simulation ($< 1.4 \mu\text{m}$). However, for more energetic major and minor element K lines (e.g., K, Ca, Ti, and Fe), the differences between XRF and EDS depth resolutions diverge nonlinearly (Additional file 1: Figure S2A). The nonlinear increase in information depth for trace elements continues for Cr, Mn, Cu, Zn, Ga, Rb, Sr, Y, Zr, and Nb, with

increasing K line X-ray energies (Additional file 1: Figure S2B). The highest atomic number trace element examined in this study is Ba, and its emission depth is similar to that for low Z first row transition metals (e.g., Ti) given its concentration is measured using the L line X-ray at lower energy.

Micro-XRF stage scan images reveal that Zn, Zr, and Ti, are enriched in the dark glass while Ba, Si, and Rb are enriched in the clear glass (Fig. 8A–C). The distribution of Ti depicts a thin film of dark glass along the uppermost margin of the specimen coating both quartz and clear glass (Fig. 8A). Zr hotspots appear throughout both glasses highlighting the presence of surficial and buried zircon (ZrSiO_4) crystals (Fig. 8B). The sum of X-rays with energies less than the Rh K line source offers a view of the specimen that may resemble a BSE image, and as such may be useful as a navigational tool for ex situ XRF imaging studies, albeit with poorer contrast between low mean atomic number phases (Fig. 8D). The sensitivity of XRF can be demonstrated by spectral resolution of a trace Ba in the presence of a major to minor concentrations of Ti, while high energy trace element X-rays are significantly less convolved (Fig. 8E–G). To determine the practical limits of trace element imaging a second μ XRF stage scan was conducted using a $100 \mu\text{m}$ Al filter. Comparative trace Zn images show that the low sensitivity (i.e., peak/background) can be improved by a factor of three using a filtered Rh source allowing for the ability to distinguish low concentration phases ($< 190 \text{ ppm}$) that differ by 100 ppm (Fig. 9A–C). A consequence of using a filtered X-ray source is the elimination of low energy diffraction artifacts, which in turn allows for the detection of trace Ti, along with suppression of higher energy diffraction in the X-ray spectrum (Fig. 9D).

Targeted imaging and analysis

Imaging and analysis of the Broborg hillfort glasses that followed overview stage-scans included: (1) higher spatial resolution EDS beam scanning with correlated multi-spectral CL imaging, and (2) quantitative EDS and μ XRF point analysis. At higher spatial resolution the interfacial region between a quartz grain and the dark glass reveals the dark glass is comprised of an intergrowth of plagioclase and FeMgCa-rich quench crystals, likely Ca-pyroxene, within a residual glass bordering a smooth quartz

(See figure on next page.)

Fig. 8 Stage scan μ XRF images, extracted spectra, and deconvolved spectral features of major, minor, and trace elements. **A** Ba (red), Si (blue), and Ti (green) X-ray image overlay. Small white arrows depict dark melt coating the specimen exterior, and larger black arrows highlight Ba- and Ti-rich regions of clear and dark glasses respectively. **B** Si (blue) and Zr (yellow) X-ray image overlay showing Zr hotspots. **C** Si (green), Zn (red), and Rb (blue) X-ray image overlay where black arrow highlights a diffraction artifact (see Fig. 9). **D** image of the sum of all X-rays with energies between 1 and 18 keV. **E** extracted spectra from Ti-rich and Ba-rich regions highlighted in **A**. **F** Deconvolved trace Ba signal in the presence of significantly greater Ti counts. **G** Deconvolved peaks for trace elements with high energy X-ray lines

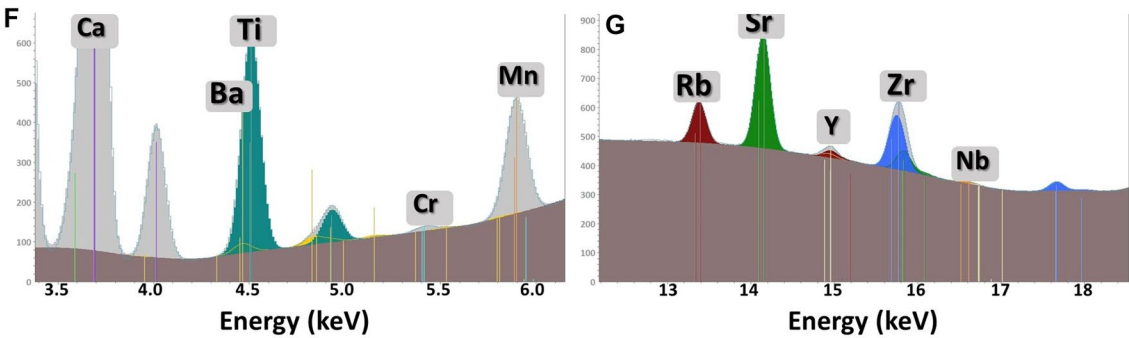
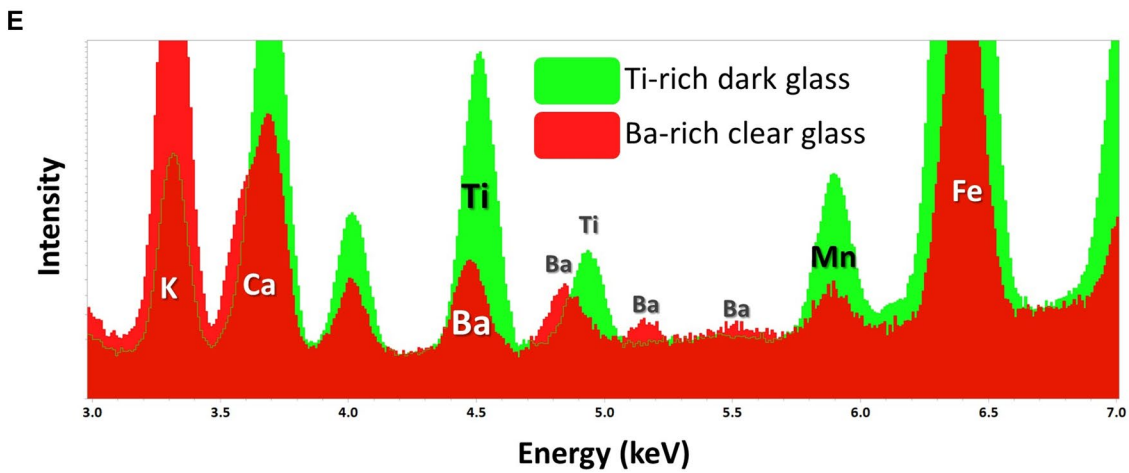
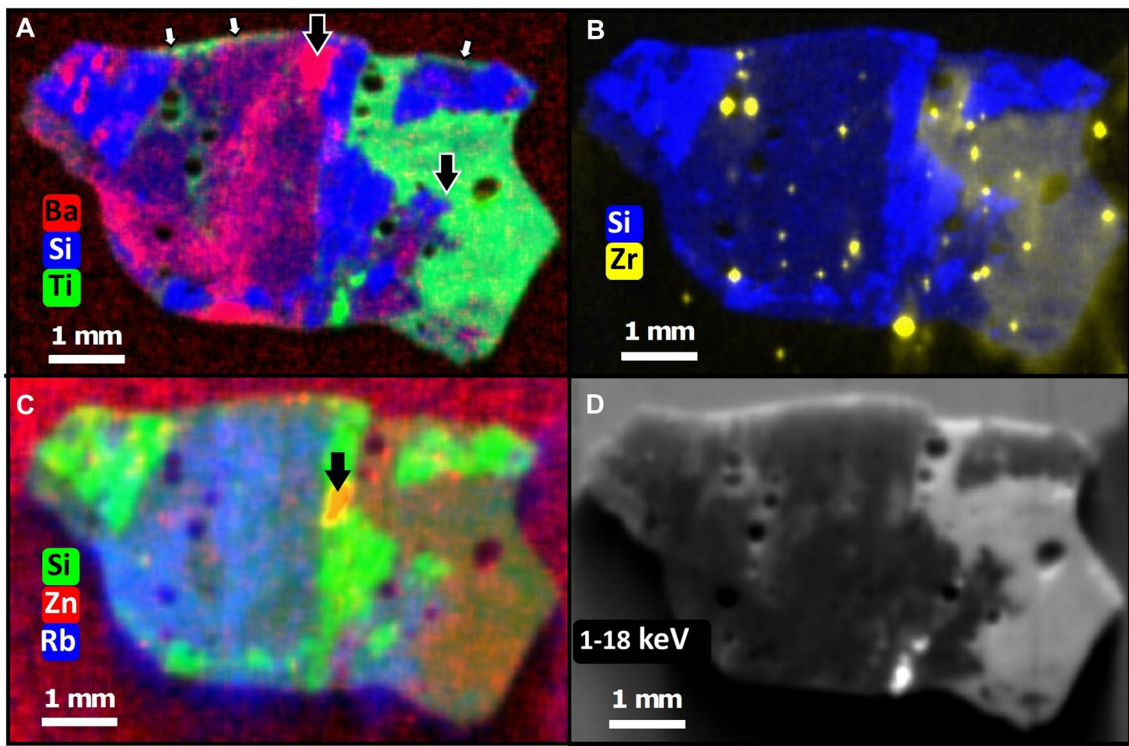
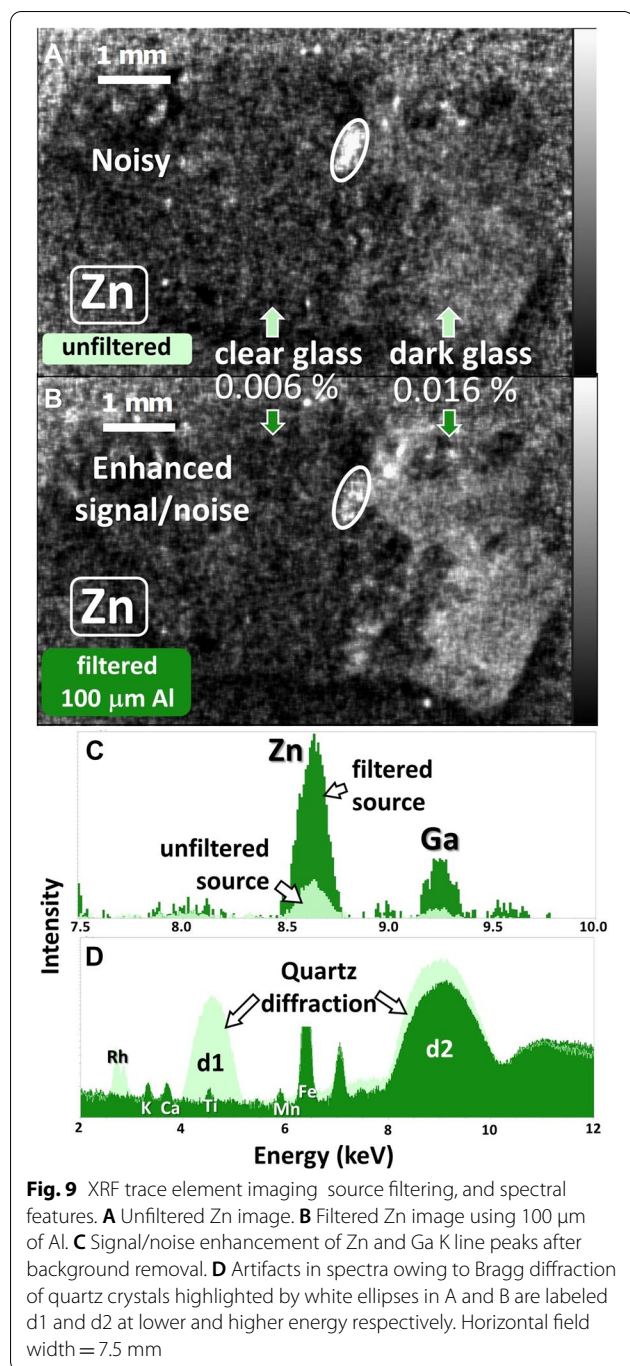


Fig. 8 (See legend on previous page.)



interface (Fig. 10A, B). CL imaging in the visible, or red–green–blue (RGB), is a function of intrinsic luminescence coupled with trace impurity activated luminescence in natural phases [40, 41] and distinguishes these phases as quartz (red), plagioclase (violet), FeMgCa

dendrites (non-luminescent) likely augite $[(\text{Ca})(\text{Mg},\text{Fe},\text{Al})(\text{Si},\text{Al})_2\text{O}_6]$, and residual glass (light blue and green) (Fig. 10C, D).

Information derived from above stage-scans was used to identify homogeneous regions of the dark and clear glasses (Additional file 1: Figure S3) for co-located EDS and μXRF quantitative point analysis (Table 1; Additional file 1: Tables S2–S5). Major and minor elements presented in Table 1 represent standards-based EDS and FP-based μXRF quantification with a comparison of results obtained for well-characterized materials presented in Additional file 1: Table S1. A graphical comparison of major, minor, and trace element compositions for the dark and clear glasses is shown in Fig. 11 where nine elements are enriched in the dark glass and eight are enriched in the clear glass. However, the degree of enrichment in the dark glass for Ti, Fe, Mg, Ca, P, Mn, Zn, Y, and Zr is significantly greater than that for Si, Al, Na, K, Ga, Rb, Sr, and Ba in the clear glass (Fig. 11). A multi-element ratio plot, comprised of major, minor, and trace elements shows normalized mean dark and clear glass compositions, where larger ions are enriched in the clear glass, and conversely, smaller ions are enriched in the dark glass (Fig. 12A). The same plot is used to compare the dark glass to bulk rock compositions for amphibolites (a rock comprised of amphibole, plagioclase feldspar, quartz, and biotite) found at Broborg [21] (Fig. 12B). While the multi-element ratio patterns are not entirely dissimilar, the dark glass is enriched relative to the bulk amphibolites for all elements apart from Ba. The coupled data from co-located EDS and μXRF quantified analyses allows one to probe such elemental relationships for a large dynamic range of elemental concentrations using the tandem analysis method.

The mean glass composition for clear and dark glasses was also used to compute anhydrous viscosities for Fe-bearing silicate melts [43]. Temperatures used for the calculation were taken as the mean of the range reported from Fe–Mg exchange between olivine and dark melt (1048 $^{\circ}\text{C}$), as well as the mean of liquidus temperatures for the clear melt (1068 $^{\circ}\text{C}$) as previously determined by Kresten et al. [20] (Fig. 13). Both temperatures result in an estimate of the dark melt being less viscous than the clear melt by a factor 74 \times during the hillfort vitrification event, and this viscosity difference is relatively insensitive to a broad range of possible melt temperatures. However, whether the dark and clear melts were simultaneously molten cannot be determined from our data.

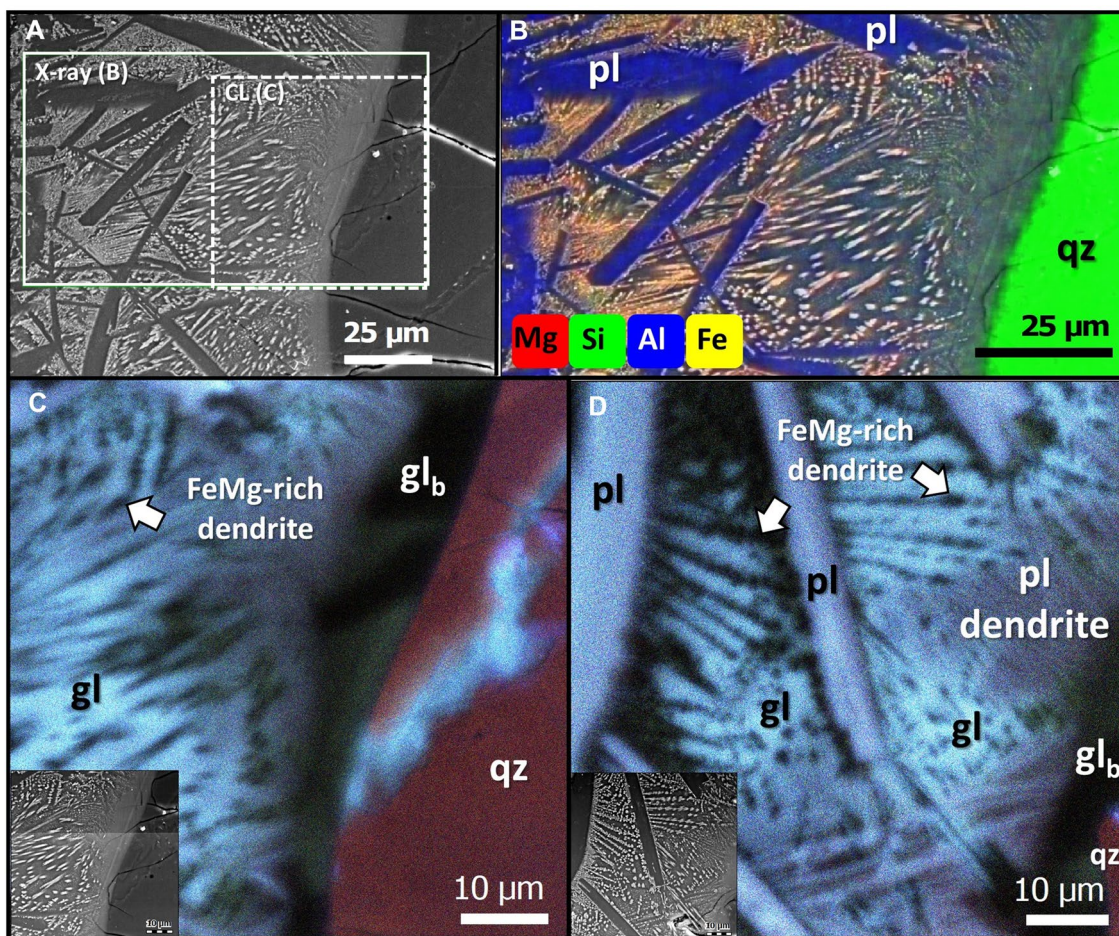


Fig. 10 Beam scan images of quartz-dark glass interface. **A** electron image of interface depicting the EDS image (white rectangle) and CL image (dashed white square) regions. **B** EDS X-ray overlay of Mg (red), Si (green), Al (blue), and Fe (yellow) highlighted in **A**. **C** RGB CL image highlighted in **A** showing CL distinguishing two glasses, blue in the matrix and green in the boundary layer with quartz. **D** RGB CL image of adjacent interface zone showing intergrowth of blue-violet plagioclase blades and non-luminescent FeMg dendrites. Abbreviations for labeled phases include plagioclase (pl), quartz (qz), glass (gl), and boundary layer glass (gl_b)

Discussion

Broborg hillfort glasses

The quantitative analyses presented here represent the most complete effort to characterize chemical differences between the dark and clear glasses found at Broborg hillfort with respect to an increased dynamic range of element concentrations. While the compositions reported here by no means represent the range of glass chemistry found at Broborg, they offer insight into conditions for a single portion of the hillfort rampart. Major and minor element patterns compare favorably to earlier electron beam studies with some notable differences: (1) dark glass compositions reported previously are enriched in MgO and CaO and depleted in SiO₂, Na₂O, and K₂O relative to the dark glass in BB1b [18, 21], and (2) the composition of a selected clear glass composition is within

uncertainty of the mean clear glass value reported here for SiO₂, CaO, TiO₂ and outside of 1 σ values for Fe₂O₃, K₂O, and P₂O₅ [18].

The large difference in computed anhydrous viscosities between the melts, suggesting approximately a 74-fold decrease in resistance to flow for the dark melt relative to the clear melt estimated for specimen BB1b, is consistent with our laboratory observation of a thin film of dark glass coating the stone exterior. The computed viscosity for the dark melt at 1048 °C of 4.5 Pa·s is equivalent to that for pine honey with 21% moisture at 25 °C of 4.8 Pa·s [44] and is thus in good agreement with field observations at Broborg where dark melts are noted to coat rocks and additionally form melt “drips” compared with clear glasses found localized in situ in the vitrified zone of the rampart [17, 20, 21].

Table 1 Quantitative EDS and μ XRF point analyses for the dark and clear glasses

	Oxide (kg/kg)	Dark glass			Clear glass				
		Mean	σ	n	Mean	σ	n		
EDS	SiO ₂	55.9	±	1.2	23	63.3	±	1.7	26
	TiO ₂	2.0	±	0.2	23	0.1	±	0.1	26
	Al ₂ O ₃	13.8	±	0.7	23	20.4	±	1.6	26
	Fe ₂ O ₃ ^{total}	11.0	±	1.0	23	0.3	±	0.2	26
	MgO	3.3	±	0.2	23	0.2	±	0.0	26
	CaO	6.1	±	0.6	23	1.1	±	0.6	26
	Na ₂ O	3.6	±	0.2	23	5.4	±	0.2	26
	K ₂ O	2.1	±	0.5	23	7.3	±	0.5	26
	P ₂ O ₅	0.8	±	0.2	23	0.1	±	0.0	26
	∑ e-beam	98.7				98.1			
	∑ XRF oxides	1.128				0.399			
	Total	99.8				98.5			
μ XRF	element (kg/kg)								
	Cr	0.003	±	0.001	11	0.002			1
	Mn	0.253	±	0.020	20	0.028	±	0.016	26
	Cu					0.003			2
	Zn	0.016	±	0.003	20	0.006	±	0.0017	11
	Ga	0.004	±	0.002	20	0.005	±	0.0014	18
	Rb	0.015	±	0.002	20	0.032	±	0.018	26
	Sr	0.053	±	0.005	20	0.078	±	0.048	26
	Y	0.009	±	0.0012	20	0.001			2
	Zr	0.113	±	0.025	20	0.002	±	0.0004	11
	Nb	0.006	±	0.0009	20				
	Ba	0.009	±	0.006	19	0.117	±	0.045	26
	Hf	0.011			2				
	Pb					0.023			1
	Th	0.003			2	0.009			2

Major and minor elements performed by EDS standards-based analysis and trace elements by FP-based μ XRF; uncertainties are listed at 1 σ . EDS analyses expressed as kg oxide per kg glass (mass %) and μ XRF analyses expressed as kg element per kg glass (mass %, $\times 10^6$ ppm) and total iron expressed as Fe₂O₃

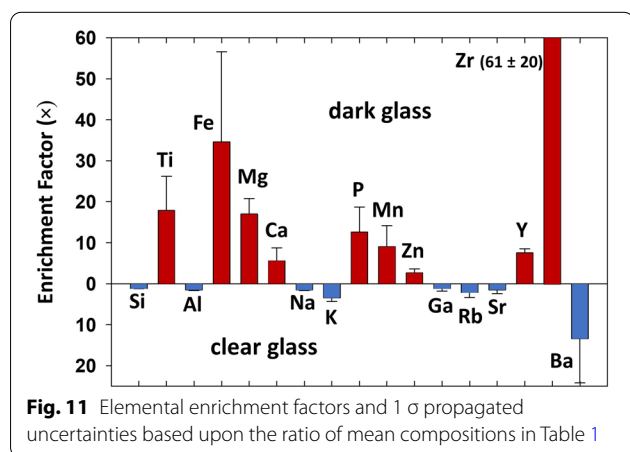
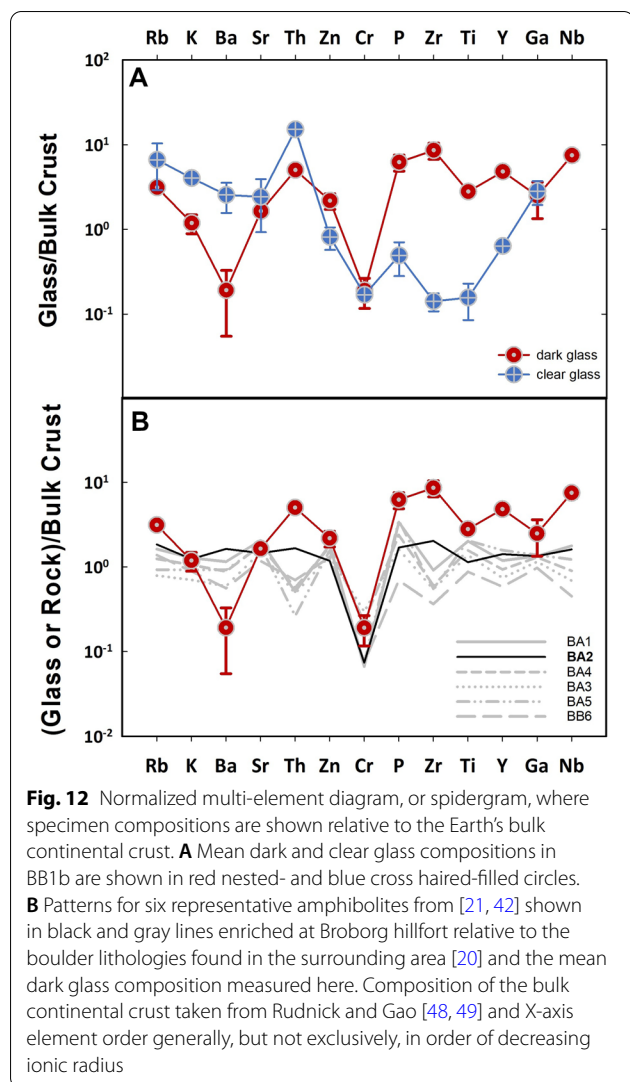


Fig. 11 Elemental enrichment factors and 1 σ propagated uncertainties based upon the ratio of mean compositions in Table 1

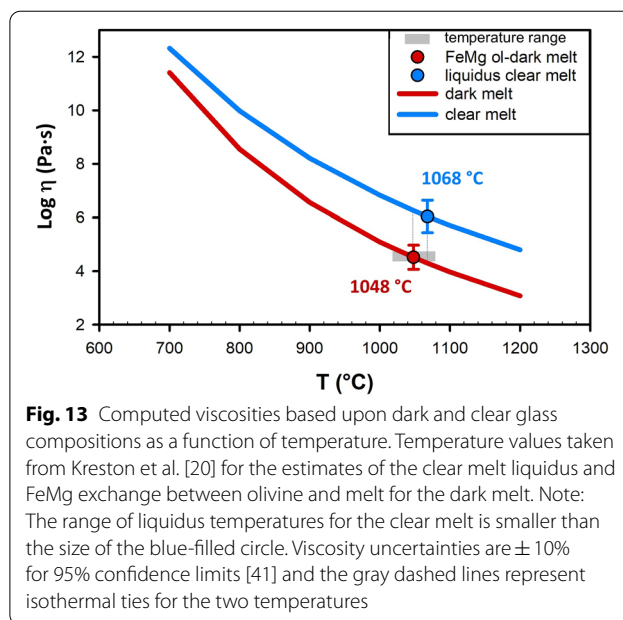
The mean clear glass composition presented here is in good agreement with the major and minor elements for the experimentally derived clear glass compositions obtained by partial melting of granitoid rocks from the hillfort [21], and supports the earlier suggestion that clear glasses from Broborg generally result from nonequilibrium partial melting of the feldspathic component of granitic gneiss [18, 20]. The mean dark glass composition we report is generally consistent with, but not an exact compositional match for the experimental glasses derived from partial melting of amphibolite [21]. The field association noted for amphibolite on the rampart with dark glass at Broborg has been noted as unequivocal, and the dark stones are found in anomalous proportions relative to the abundant granitoid boulders surrounding the hillfort [18, 20]. Interestingly, our multielement plot shows



a similar pattern between bulk amphibolites from Broborg and the dark glass from BB1b (Fig. 12 B) with the exception of depleted Ba values which can be related to retention of plagioclase feldspar during partial melting [45]. As such, these new element patterns support the earlier field, analytical, and experimental studies that link the dark glass to the incongruent melting of amphibolite as the most likely source to form the vitreous cement in the hillforts' rampart [18, 20, 21].

Value of correlated stage-scan imaging

Registered imagery from EDS and μ XRF stage scanning collected in tandem offers a new method to evaluate specimens with microstructural features that span millimeters to centimeters in scale. These combined hyperspectral data sets cover a large fraction of the energy



spectrum from soft X-rays (e.g., B, C, O) to high energy K lines (e.g., Zr, Nb, Mo) with the realization that high energy X-rays may be generated from tens to hundreds of times deeper within specimens relative to EDS emission depths. Such complete microchemical characterization enables an elemental context to be established for follow-up studies using a variety of ancillary methods to probe materials in the SEM for defects, crystallographic orientation, and atomic resolution studies using CL, electron backscattered diffraction (EBSD), and 3D focused ion beam sectioning and lift out for transmission electron microscopy (3D FIB/TEM).

Archaeometric studies of metal, ceramic, and mixed materials that demand nondestructive or minimally destructive analysis will benefit from this coupled approach, particularly those that require larger examination areas; for example, durability of ancient concrete [46, 47]. Another important role tandem analysis can fill is screening specimens proposed for synchrotron studies. Given the high value of time on beam lines at light source facilities, advanced knowledge of a material obtained from laboratory μ XRF and EDS can be invaluable for optimizing measurements performed with high brightness sources, especially for synchrotron mapping studies.

Conclusions

Correlated EDS and μ XRF stage scan imaging using the tandem system for a Broborg vitrified hillfort specimen reveals an assemblage dominated by FeMgCa-enriched dark glass, SiAlK-clear glass, quartz, spinel, Ca-feldspar, apatite, and zircon. MVSA output obtained from the EDS

hyperspectral data allows for the determination of area fractions for chemical phases over a large area covering tens of square millimeters at micrometer-scale resolution. Dark and clear glasses compositions define distinct populations and differences in their computed viscosities at vitrification temperatures align well with laboratory and field observations.

While used to illustrate an overview analysis of late iron age glasses at a vitrified hillfort, the coupled imaging and analysis technique described here is broadly applicable to a variety of cultural heritage materials and enables routine minor and trace element data collected via μ XRF that complements traditional major element EDS output. This new capability for the SEM platform allows for a workflow that includes a nondestructive microchemical overview via stage scanning prior to detailed studies performed either *in situ*, or *ex situ*, for example at synchrotron facilities.

Abbreviations

μ XRF: Micro-X-ray fluorescence; EDS: Energy dispersive spectrometry; CL: Cathodoluminescence; SEM: Scanning electron microscope; DOE: Department of Energy; US: United States; tandem: The ANalytical Dual bEam Microscope; PNNL: Pacific Northwest National Laboratory; MVSA: Multivariate statistical analysis; AXSIA: Automated eXpert Spectrum Image Analysis.

Supplementary Information

The online version contains supplementary material available at <https://doi.org/10.1186/s40494-022-00707-4>.

Additional file 1: Note S1. Multivariate statistical analysis (MVSA) details. **Figure S1.** Higher resolution EDS stage-scanned maps. **Figure S2.** Emission depths for X-rays. **Figure S3.** Quantitative analysis locations. **Table S1.** Compositions of well characterized materials. **Table S2.** Major and minor element composition of dark glass by EDS. **Table S3.** Major and minor element composition of clear glass by EDS. **Table S4.** Trace element composition of dark glass by μ XRF. **Table S5.** Trace element composition of clear glass by μ XRF.

Acknowledgements

We thank Anthony Guzman for preparation of the specimen at PNNL. Certain commercial equipment, instruments, or materials (or suppliers, or software) are identified in this paper to foster understanding. Such identification does not imply recommendation or endorsement by the Smithsonian Institution, or the National Institute of Standards and Technology, nor does it imply that the materials or equipment identified are necessarily the best available for the purpose.

Author contributions

EPV: conceptualization, methodology, data collection, analysis, and wrote the first draft. TL: methodology, data collection, analysis, manuscript revision. JLW: specimen acquisition/field context, manuscript revision. AAH: multivariate statistical analysis, manuscript revision. JSM: specimen acquisition/field context, manuscript revision. RS: initially conceived the overarching project, manuscript revision. CIP: specimen acquisition/field context, funds acquisition, manuscript revision. All authors read and approved the final manuscript.

Funding

This work is supported by the Smithsonian Institution, the National Institute of Standards and Technology, and partly by the United States Department of Energy (US DOE) Office of Environmental Management, International

Programs, and by the US DOE Waste Treatment and Immobilization Plant Project.

Availability of data and materials

A supplementary information file contains details regarding the MVSA analysis, higher resolution EDS maps, the compositions of well-characterized materials, X-ray emission depths, locations for quantitative analysis, major and minor element compositions by EDS, and trace element compositions by μ XRF.

Declarations

Competing interests

The authors declare that they have no competing interests.

Author details

¹Museum Conservation Institute, Smithsonian Institution, Suitland, MD 20746, USA. ²Materials Measurement Laboratory, National Institute of Standards and Technology, Gaithersburg, MD 20899, USA. ³School of Mechanical and Materials Engineering, Washington State University, Pullman, WA, USA. ⁴Luleå University of Technology, SE-971 87 Luleå, Sweden. ⁵Pacific Northwest National Laboratory, 902 Battelle Blvd, Richland, WA 99352, USA.

Received: 6 December 2021 Accepted: 28 April 2022

Published online: 16 June 2022

References

- Kane RE, Liddicoat RT. The Biron hydrothermal synthetic emerald. *Gems Gemology*. 1985;21(3):156–70.
- Bush MA, Miller RG, Norrlander AL, Bush PJ. Analytical survey of restorative resins by SEM/EDS and XRF: databases for forensic purposes. *J Forensic Sci*. 2008;53(2):419–25. <https://doi.org/10.1111/j.1556-4029.2007.00654.x>.
- Cao Y, Linnen R, Good D, Samson I, Epstein R. The application of portable XRF and benchtop SEM-EDS to Cu-Pd exploration in the Coldwell Alkaline Complex, Ontario, Canada. *Geochem Explor Environ Anal*. 2016;16(3–4):193–212. <https://doi.org/10.1144/geochem2015-394>.
- Orange M, Le Bourdonnec F-X, Bellot-Gurlet L, Lugliè C, Dubernet S, Bressy-Leandri C, Scheffers A, Joannes-Boyau R. On sourcing obsidian assemblages from the Mediterranean area: analytical strategies for their exhaustive geochemical characterisation. *J Archaeol Sci Rep*. 2017;12:834–44. <https://doi.org/10.1016/j.jasrep.2016.06.002>.
- Freitas RP, Coelho FA, Felix VS, Pereira MO, de Souza MAT, Anjos MJ. Analysis of 19th century ceramic fragments excavated from Pirenópolis (Goias, Brazil) using FT-IR, Raman, XRF and SEM. *Spectrochim Acta Part A Mol Biomol Spectrosc*. 2018;193:432–9. <https://doi.org/10.1016/j.saa.2017.12.047>.
- Smith D. Handheld X-ray fluorescence analysis of Renaissance bronzes: practical approaches to quantification and acquisition. *Handheld XRF for art and archaeology*. Leuven, Belgium: Leuven University Press; 2012. p. 37–74.
- Torpy A, MacRae C, Fazey P, Wilson N, editors. Microbeam x-ray fluorescence in an electron microprobe. In: ACEM17 Australian Conference on Electron Microscopy; 2002 4–8 Feb.; Adelaide, SA (Australia): The Australian Society For Electron Microscopy, Inc.; 2002.
- Torpy A, MacRae C, Harrowfield I, Rummel P, editors. Development of a Dual Excitation X-ray/Electron Microprobe (DEXREM). Sydney, NSW: Australian Microbeam Analysis Society VI; 2001 14–16 Feb., 2001, Australia; 2001.
- Janssens K, Vincze L, Rubio J, Adams F, Bernasconi G. Microscopic X-ray fluorescence analysis. Invited lecture. *J Anal Atom Spectrom*. 1994;9(3):151–7. <https://doi.org/10.1039/JA9940900151>.
- Gao N, Ponomarev IY, Xiao Q, Gibson W, Carpenter D. Monolithic polycapillary focusing optics and their applications in microbeam x-ray fluorescence. *Appl Phys Lett*. 1996;69(11):1529–31. <https://doi.org/10.1063/1.117994>.
- Jindong X, Yejun H, Xunliang D, Qiuli P, Yiming Y. The monolithic X-ray polycapillary lens and its application in microbeam X-ray fluorescence. *J Anal At Spectrom*. 1999;14(3):391–4. <https://doi.org/10.1039/A806836D>.

12. Bjeoumikhov A, Langhoff N, Wedell R, Beloglazov V, Lebed'Ev N, Skibina N. New generation of polycapillary lenses: manufacture and applications. *X-Ray Spectrom Int J*. 2003;32(3):172–8. <https://doi.org/10.1002/xrs.587>.
13. Witherspoon K, Cross B, Lamb R, Sjöman P. Advancements in integrated micro-XRF in the SEM. *Microsc Microanal*. 2009;15(S2):180–1. <https://doi.org/10.1017/S1431927609098304>.
14. Haschke M, Boehm S. Micro-XRF in scanning electron microscopes. *Advances in imaging and electron physics*, vol. 199. Cambridge, MA: Elsevier; 2017. p. 1–60. <https://doi.org/10.1016/bs.aiep.2017.01.001>.
15. Cross BJ, Witherspoon K. Integrated XRF in the SEM. *Microsc Microanal*. 2004;10(S02):104–5. <https://doi.org/10.1017/S1431927604885684>.
16. Sharps MC, Martinez MM, Brandl M, Lam T, Vicenzi EP. A dual beam SEM-based EDS and micro-XRF method for the analysis of large-scale Mesoamerican obsidian tablets. *J Archaeol Sci Rep*. 2021;35: 102781. <https://doi.org/10.1016/j.jasrep.2020.102781>.
17. Englund M. Broborg hillfort a research study of the vitrified wall. *Arkeologerna*; 2018. Contract No.: Report 2018. p. 103.
18. Kresten P, Ambrosiani B. Swedish vitrified forts—a reconnaissance study. *Fornvännen J Swed Antiqu Res*. 1992;1–17.
19. Sjöblom R, Hjärthner-Holdar E, Pearce CI, Weaver JL, Ogenhall E, Mc Cloy JS, Marcial J, Vicenzi EP, Schweiger MJ, Kruger AA. Assessment of the reason for the vitrification of a wall at a hillfort. The example of Broborg in Sweden. *J Archaeol Sci Rep*. 2022;43:103459. <https://doi.org/10.1016/j.jasrep.2022.103459>.
20. Kresten P, Kero L, Chyessler J. Geology of the vitrified hill-fort Broborg in Uppland, Sweden. *Geologiska Föreningen i Stockholm Förhandlingar*. 1993;115(1):13–24. <https://doi.org/10.1080/11035899309454825>.
21. Mc Cloy JS, Marcial J, Clarke JS, Ahmadzadeh M, Wolff JA, Vicenzi EP, Bollinger DL, Ogenhall E, Englund M, Pearce CI, Sjöblom R, Kruger AA. Reproduction of melting behavior for vitrified hillforts based on amphibolite, granite, and basalt lithologies. *Sci Rep*. 2021;11(1):1272. <https://doi.org/10.1038/s41598-020-80485-w>.
22. Weaver JL, Pearce CI, Sjöblom R, Mc Cloy JS, Miller M, Varga T, Arey B, Conroy M, Peeler D, Koestler R, De Preist P, Hjärthner-Holdar E, Ogenhall E, Kruger AA. Pre-Viking Swedish hillfort glass: a prospective long-term alteration analogue for vitrified nuclear waste. *Int J Appl Glas Sci*. 2018;9(4):540–54. <https://doi.org/10.1111/jjag.12351>.
23. Lagerbielke E. Aspects of the development of Swedish glass manufacturing. *J Glass Stud*. 2021;63:303–20.
24. Lo Giudice A, Re A, Calusi S, Giuntini L, Massi M, Olivero P, Pratesi G, Albonico M, Conz E. Multitechnique characterization of lapis lazuli for provenance study. *Anal Bioanal Chem*. 2009;395(7):2211–7.
25. Palamara E, Das P, Nicolopoulos S, Tormo Cifuentes L, Kouloumpi E, Terlixi A, Zacharias N. Towards building a Cathodoluminescence (CL) database for pigments: characterization of white pigments. *Herit Sci*. 2021;9(1):1–14.
26. Jarosewich E, Nelen J, Norberg JA. Reference samples for electron microprobe analysis. *Geostand Newsl*. 1980;4(1):43–7. <https://doi.org/10.1111/j.1751-908X.1980.tb00273.x>.
27. Vicenzi EP, Eggins S, Logan A, Wysoczanski R. Microbeam characterization of corning archeological reference glasses: new additions to the smithsonian microbeam standard collection. *J Res Nat Inst Stand Technol*. 2002;107(6):719. <https://doi.org/10.6028/jres.107.058> (PMCID: **PMC4863856**).
28. Haschke M. Laboratory micro-X-ray fluorescence spectroscopy: Instrumentation and Applications. Ertl G, Lüth H, Mills DL, editors. Heidelberg, Germany: Springer; 2014. 978-3-319-0-4863-5
29. Ritchie NW. Spectrum simulation in DTSA-II. *Microsc Microanal*. 2009;15(5):454–68. <https://doi.org/10.1017/S1431927609990407>.
30. Wolff T. Information depth—XRF Check Bruker.com: Bruker; 2020 [Available from: <https://xrfcheck.bruker.com/InfoDepth>].
31. Parish C, Brewer L. Multivariate statistics-based segmentation methods for quantification of X-ray spectrum images. *Ultramicroscopy*. 2010;110(2):134–43.
32. Parish CM. Multivariate statistics applications in scanning transmission electron microscopy X-ray spectrum imaging. *Advances in imaging and electron physics*, vol. 168. Elsevier; 2011. p. 249–95.
33. Titchmarsh J. EDX spectrum modelling and multivariate analysis of subnanometer segregation. *Micron*. 1999;30(2):159–71.
34. Titchmarsh J, Dumbill S. Multivariate statistical analysis of FEG-STEM EDX spectra. *J Microsc*. 1996;184(3):195–207.
35. Trebbia P, Bonnet N. EELS elemental mapping with unconventional methods I. Theoretical basis: image analysis with multivariate statistics and entropy concepts. *Ultramicroscopy*. 1990;34(3):165–78.
36. Trebbia P, Mory C. EELS elemental mapping with unconventional methods II. Applications to biological specimens. *Ultramicroscopy*. 1990;34(3):179–203.
37. Kotula PG, Keenan MR. Application of multivariate statistical analysis to STEM X-ray spectral images: interfacial analysis in microelectronics. *Microsc Microanal*. 2006;12(6):538–44.
38. Otsu N. A threshold selection method from gray-level histograms. *IEEE transactions on systems, man, and cybernetics*. 1979;9:62–6.
39. Friend CR, Kirby JE, Charnley NR, Dye J. New field, analytical data and melting temperature determinations from three vitrified forts in Lochaber, Western Highlands, Scotland. *J Archaeol Sci Rep*. 2016;10:237–52. <https://doi.org/10.1016/j.jasrep.2016.09.015>.
40. Thomas WP, MacRae CM, Wilson NC, Torpy A, Lee C-TA, Student JJ, Leeman WP, Vicenzi EP. A study of cathodoluminescence and trace element compositional zoning in natural quartz from volcanic rocks: mapping titanium content in quartz. *Microsc Microanal*. 2012;18(6):1322–41. <https://doi.org/10.1017/S1431927612013426>.
41. Macrae CM, Wilson NC, Johnson SA, Phillips PL, Otsuki M. Hyperspectral mapping—combining cathodoluminescence and X-ray collection in an electron microprobe. *Microsc Res Tech*. 2005;67(5):271–7. <https://doi.org/10.1002/jemt.20205>.
42. Ogenhall E. Amphibolitic ROCKS NEAR BROBORG, Uppland. Knivsta, Sweden; 2015. Contract No.: Dnr 5.1.1-01422-2015.
43. Giordano D, Russell JK, Dingwell DB. Viscosity of magmatic liquids: a model. *Earth Planet Sci Lett*. 2008;271(1–4):123–34. <https://doi.org/10.1016/j.epsl.2008.03.038>.
44. Yanniotis S, Skaltsi S, and Karaburniotti S. (2006) Effect of moisture content on the viscosity of honey at different temperatures. *Journal of Food Engineering* 72, 372–377.
45. Singh LG, Vallinayagam G. Petrological and geochemical constraints in the origin and associated mineralization of A-type granite suite of the Dhiran Area, Northwestern Peninsular India. *Geosciences*. 2012;2(4):66–80.
46. Jackson MD, Landis EN, Brune PF, Vitti M, Chen H, Li Q, Kunz M, Wenk H-R, Monteiro PJ, Ingraffea AR. Mechanical resilience and cementitious processes in Imperial Roman architectural mortar. *Proc Natl Acad Sci*. 2014;111(52):18484–9.
47. Seymour LM, Tamura N, Jackson MD, Masic A. Reactive binder and aggregate interfacial zones in the mortar of Tomb of Caecilia Metella concrete, 1C BCE, Rome. *J Am Ceram Soc*. 2021. <https://doi.org/10.1111/jace.18133>.
48. Rudnick RL, Gao S. The Crust. In: Holland HD, Turekian KK, editors. *Treatise on geochemistry*. Elsevier; 2003. p. 1–64.
49. Rudnick R, Gao S. 4.1 - Composition of the Continental Crust. In: Holland HD, Turekian KK, editors. *Treatise on Geochemistry*, Volume 4. 2nd ed. Netherlands: Elsevier, Amsterdam; 2014. p. 1–51.

Publisher's Note

Springer Nature remains neutral with regard to jurisdictional claims in published maps and institutional affiliations.